



LAWRENCE  
LIVERMORE  
NATIONAL  
LABORATORY

# Detector design for high-resolution MeV photon imaging of cargo containers using spectral information

M.-A. Descalle, K. Vetter, A. Hansen, J. Daniels,  
S. G. Prussin

February 11, 2010

Nuclear Instrument and Methods in Physics Research section  
A

## **Disclaimer**

---

This document was prepared as an account of work sponsored by an agency of the United States government. Neither the United States government nor Lawrence Livermore National Security, LLC, nor any of their employees makes any warranty, expressed or implied, or assumes any legal liability or responsibility for the accuracy, completeness, or usefulness of any information, apparatus, product, or process disclosed, or represents that its use would not infringe privately owned rights. Reference herein to any specific commercial product, process, or service by trade name, trademark, manufacturer, or otherwise does not necessarily constitute or imply its endorsement, recommendation, or favoring by the United States government or Lawrence Livermore National Security, LLC. The views and opinions of authors expressed herein do not necessarily state or reflect those of the United States government or Lawrence Livermore National Security, LLC, and shall not be used for advertising or product endorsement purposes.

# 1 **Detector design for high-resolution MeV photon imaging of** 2 **cargo containers using spectral information**

3 Marie-Anne Descalle<sup>1</sup>, Kai Vetter<sup>2</sup>, Araina Hansen<sup>2</sup>, Joseph Daniel<sup>2</sup>, Stanley G. Prussin<sup>2</sup>

4  
5 <sup>1</sup>Physics and Life Sciences Directorate, Lawrence Livermore National Laboratory, 7000  
6 East Avenue, Livermore, California 94550

7 <sup>2</sup>Departments of Nuclear Engineering and Chemistry, University of California, Berkeley,  
8 California 94720

9  
10 Corresponding author: Marie-Anne Descalle, Lawrence Livermore National Laboratory,  
11 Physical & Life Sciences Directorate L-211, 7000 East Avenue, Livermore, CA 94550  
12 E-mail: [descalle1@llnl.gov](mailto:descalle1@llnl.gov), phone: (925) 423 9660, fax: (925) 424-5512

## 13 **Abstract**

14 Monte Carlo simulations of a pixelated detector array of inorganic scintillators for high  
15 spatial resolution imaging of 1-9 MeV photons are presented. The results suggest that a  
16 detector array of 0.5 cm x 0.5 cm x 5 cm pixels of bismuth germanate may provide  
17 sufficient efficiency and spatial resolution to permit imaging of an object with  
18 uncertainties in dimension of several mm. The cross talk between pixels is found to be in  
19 the range of a few percent when pixels are shielded by ~ 1mm of lead or tungsten. The  
20 contrast at the edge of an object is greatly improved by rejection of events depositing less  
21 than ~ 1 MeV. Given the relatively short decay time of BGO, the simulations suggest that  
22 such a detector may prove adequate for the purpose of rapid scanning of highly-shielded  
23 cargos for possible presence of high atomic number (including clandestine fissionable)  
24 materials when used with low current high duty factor x-ray sources.

25  
26 **Keywords:** Monte Carlo simulations; Container scanning; Bremsstrahlung; Inorganic  
27 scintillator; MeV photon imaging; Energy discrimination

## 28 **1. Introduction**

29 In 2007, the United States (US) Congress mandated the screening of all shipborne  
30 intermodal cargo containers arriving at US ports by the Department of Homeland  
31 Security (DHS) within the next five years, a daunting task in light of the staggering  
32 number of cargo containers entering the country by container ship.[1]

33 Of particular interest is screening for the possible presence of clandestine  
34 fissionable materials. The need to maintain the normal flow of commerce imposes severe  
35 time constraints on any proposed method of inspection, and it has thus become clear that  
36 a two-step approach would be very useful. First, a rapid primary screening should be  
37 highly efficient both in time and effectiveness and should pass the overwhelming portion  
38 of containers that contain no such clandestine material in reasonable quantity, thus  
39 isolating a small subset of possibly suspicious cargos. Suspect containers would then be  
40 sent through a secondary screening with active interrogation for definitive determination  
41 of the presence or absence of special nuclear material (SNM).[2][3][4][5] Active  
42 interrogation would probe the cargo with neutron or photon beams to, depending on the

1 application, generate images of the cargo content, obtain characteristic spectral  
2 information, or, to induce fission or produce nuclear resonance fluorescence (NRF) to  
3 generate and detect definitive signatures.

4 DHS specifications for cargo advanced automated radiography systems (CAARS)  
5 suggest that such systems should be capable of detecting a  $100 \text{ cm}^3$  cube of high-Z  
6 material ( $Z \geq 72$ , mass  $\sim 2 \text{ kg}$ ) behind up to 25.4 cm of steel hidden anywhere in an  
7 intermodal cargo container.[6][7] To minimize the impact on the flow of commerce, the  
8 time required to perform a complete scan of a container should be less than one minute.  
9 Finally, the desired spatial resolution is 0.125 in (0.318 cm) and the system should have a  
10 contrast specificity greater than 2% and a contrast accuracy of  $\pm 1\%$ .

11 With these specifications in mind, we are investigating the feasibility of high-  
12 resolution MeV photon imaging as a means of accurate determination of the linear  
13 attenuation coefficient of an object and hence the atomic number of an elemental object.  
14 Our approach is based on radiographic measurements using high duty factor  
15 commercially-available bremsstrahlung sources such as Rhodotrons.[8][9]

16 Monte Carlo simulations reported by Quiter et al. demonstrated the feasibility of a  
17 method for high-resolution x-ray imaging of cargo containers using a bremsstrahlung  
18 beam ( $E_{\beta, \text{max}} \sim 9 \text{ MeV}$ ), and a schematic 15-cm thick plastic scintillator. The scattered  
19 photon contribution to the detected signal could be greatly reduced by imposing an  
20 energy threshold of  $\sim 3 \text{ MeV}$  with the detector operating in pulse counting mode.[10] The  
21 results showed that spheres of metallic uranium or plutonium with masses as small as  $\sim$   
22 0.1 kg might be imaged and reasonably accurate linear attenuation coefficients extracted  
23 in at least some cases in homogeneous cargos.

24 In the present manuscript, we describe a proposed design for a high-resolution  
25 imaging detector with characteristics very different from a plastic scintillator to span the  
26 range of possible materials properties. We have considered both bismuth germanate  
27 (BGO,  $\rho = 7.13 \text{ g cm}^{-3}$ ) and cadmium tungstate ( $\text{CdWO}_4$ ,  $\rho = 8.0 \text{ g cm}^{-3}$ ) because of their  
28 higher densities that should lead to significantly improved spatial resolution relative to  
29 plastic. We also have investigated the effects of photon interactions and electron transport  
30 on the contrast that can be expected with various energy thresholds in the range  $0.5 \leq E_d$   
31  $\leq 4 \text{ MeV}$ . In Section 2, we describe the three models used in Monte Carlo particle  
32 transport simulations to study several parameters of importance to the detector design. In  
33 Section 3, we present and analyze the results of the simulations. Section 4 concludes with  
34 a summary of the detector design.

## 35 **2. Monte Carlo Simulations**

36 To accurately measure the dimensions of an object to an uncertainty on the order  
37 of 0.25 cm, we have considered an initial pixel dimension of 0.5 cm x 0.5 cm. The  
38 detector thickness was set to 5 cm to provide an interaction probability of 0.9 to 0.8 as the  
39 incident photon energy varies in the range 1.0 to 9.0 MeV.

40 Monte Carlo simulations were performed with MCNP5 run on an AMD Linux  
41 cluster (CHAOS4.2, 2.4 GHz, 64 processors) with the ENDF/B-VII photon cross-section  
42 library. [11][12][13] The computations included photon and electron transport, and the  
43 production and transport of secondary bremsstrahlung radiation. In order to focus on the  
44 fundamental transport physics, the majority of the simulations were performed with

1 monoenergetic beams. Transport histories were followed until the energy of the radiation  
2 fell below 1 keV and the results were tallied as pulse height spectra in 100 keV bins.

3 The energy deposition in radial zones about the incident direction of  
4 monoenergetic photons was examined in a first set of simulations with pencil beams  
5 centered on and normal to one face of a cubical detector, 5 cm in length (Figure 1).  
6 Incident photon energies were increased from 1 to 9 MeV in 2 MeV increments and the  
7 total energy deposited was tallied within cylindrical volumes of radii  $r$  equal to 0.5 mm,  
8 1.0 mm, 2.0 mm, etc., over the range 1 to 1.5 cm.

9 The second model was developed in order to assess the effect of various energy  
10 discrimination levels on spatial resolution for the recorded events. One half of the face of  
11 the BGO crystal model used in the first simulations was covered by a totally absorbing  
12 slab, as shown in Figure 2. The surface was irradiated uniformly with a 4 cm x 4 cm  
13 square beam normal to the surface. Pulse height spectra and the total energy deposited  
14 were recorded in voxels with dimensions 0.1 cm x 0.1 cm x 5 cm aligned in a vertical  
15 central line normal to the edge of the totally absorbing slab.

16 A significant effect that can limit the quality of an extracted attenuation  
17 coefficient is the energy deposition in a pixel due to an initial interaction in an adjacent  
18 pixel (crosstalk). To assess the magnitude of this effect, simulations were performed with  
19 a third model consisting of a 3 x 3 array of 5 mm x 5mm square pixels of 5 cm length,  
20 separated by a 1 mm thick grid of shielding material (Figure 3). The crystals were defined  
21 as BGO, and the grid space was filled either with 1 mm of tungsten, 1 mm of lead, or 0.5  
22 mm of lead between two layers of 0.25 mm thick plastic. As a "worst case", a grid  
23 composed of 1 mm of air was also modeled. The photon source was first represented both  
24 as a monoenergetic beam and then as the 9 MeV endpoint bremsstrahlung beam defined  
25 by Quiter et al., centered on and normal to the face of the central crystal. The cross-  
26 section of the beam was a square of 6 mm x 6 mm and covered the crystal and one half of  
27 the grid area surrounding it. For reference, a pencil beam centered on the central pixel  
28 was also simulated to provide a comparison to the simulations discussed above. In all  
29 cases, the energy deposited in each crystal and the energy spectrum for the total currents  
30 passing through the crystal interfaces were recorded.

### 31 **3. Results and discussion**

#### 32 **3.1 Detector material**

33 The energy deposition in regions of increasing radial dimensions are shown in  
34 Figure 4 for both BGO and  $\text{CdWO}_4$ , where monoenergetic pencil beams were incident on  
35 the center of a 5 cm cubical crystal. Clearly, the response of the two materials is almost  
36 identical as might be expected from their similar mass attenuation coefficients. Our  
37 choice of BGO as the detector material for further study is based primarily on the  
38 differences in the decay times of the scintillations in the materials and the likelihood that  
39 practical applications will experience large interaction rates in individual pixels. The  
40 average decay time for  $\text{CdWO}_4$  is  $\sim 9.1 \mu\text{s}$  compared to  $\sim 0.3 \mu\text{s}$  for BGO. [14] Although  
41 the light yield from  $\text{CdWO}_4$  is significantly larger than that for BGO and thus leads to a  
42 better energy resolution, the continuous nature of the photon spectrum expected from  
43 bremsstrahlung beams makes this advantage much less significant relative to the shorter  
44 average decay time of BGO.

### 3.2 Pixel dimension

The energy deposition within cylindrical regions of increasing radius for varying source energies is shown in Figure 5 as the ratio of the energy deposited to the incident photon energy (upper panel) and as the fraction of the total energy deposited in the crystal (lower panel), for the 5 cm BGO crystal. As seen in the upper panel, a 1 MeV photon deposits ~ 60% of its energy within a radius of 2.5 mm, while photons of energy 3 to 9 MeV deposit ~ 50% of their energy in the same radial dimension. As the radius increases to ~ 4 mm, only about 60% of the initial energy is deposited and there is very little gain with further increase in radius except for the lowest-energy photons.

The rather high efficiency for energy deposition of the higher-energy photons is dominated by both the increasing cross-section for pair production and the strong forward peaking of the incoherent scattering cross-section at these energies. For reference, the ranges of 1 and 9 MeV electrons in BGO in the continuous slowing down approximation (CSDA) are approximately 1 and 8 mm, respectively.[15]

Of direct interest to the ability to discriminate against scattered radiation is the fraction of total energy deposited by the average photon in various radial dimensions. As shown in the lower panel, photons in the energy range 1 to 9 MeV deposit ~ 70 to 85% of the total energy deposited within ~ 2.5 mm of their incident trajectories. This indicates that a 0.5 cm x 0.5 cm pixel dimension for an imaging detector will be reasonably efficient in representing the spectral distribution of an incident photon spectrum up to at least 9 MeV. The choice of BGO over plastic for the detector material improves the spatial resolution of an image by a factor of about three when compared to the 1.5 cm x 1.5 cm pixel dimension of the plastic scintillator modeled by Quiter et al.

### 3.3 Energy spectra

To gain a general understanding of the energy spectra deposited in the BGO cube, the intensity distributions were studied as a function of energy threshold in the range 0 to 9 MeV. Monoenergetic pencil beams of 1 to 9 MeV in 2 MeV increments were considered and the energy deposited within a 3 mm radius cylindrical volume about the beam axis were recorded. The fraction of total counts is shown in Figure 6 as a function of threshold energy. For an incident energy of 1 MeV, which interact predominantly by incoherent scattering and photoelectric absorption, ~ 9% of the photons exit without interacting in the crystal, and the fraction of total counts decreases rather sharply as the threshold energy increases beyond several hundred keV.

For incident photons with energy greater than the pair production threshold, about 23% escapes from the crystal uncollided, and both counts and energy deposited decrease much less rapidly with increasing threshold energy to just below the energy of the single escape peak. For example, at a threshold of 2 MeV, the number of counts for 3 MeV incident photons is about 53% of the total number of counts, it is 88% for 5 MeV photons, and ~ 94% for 7 and 9 MeV photons. The results discussed above are consistent with the 3 MeV energy threshold chosen by Quiter et al. but they strongly indicate that the threshold might be reduced to 2.0 to 2.5 MeV, assuming that the contribution from scattered photons can be determined with reasonable accuracy.

### 3.4 Image contrast

The ability to distinguish an isolated region of high attenuation within an image, and thus the ability to determine accurately the dimension of an object, is limited by contrast. In general, contrast will be dependent upon the divergence of an incident photon beam, the attenuation characteristics of an object, the scattering characteristics of the medium in which the object is embedded, and the characteristics of the photon detector.

To study the effect of energy threshold on image contrast for the present application, we have performed a simulation in which a totally absorbing medium shielded one half of a BGO crystal of 5 cm thickness as shown in Figure 2. The system was irradiated with a uniform planar beam of photons with an energy distribution representative of a 9 MeV endpoint energy bremsstrahlung spectrum. The BGO was subdivided into pixels of 1 mm x 1 mm. The counts per source photon ( $\text{sp}^{-1}$ ) registered in the central line of pixels normal to the edge of the pure absorber were recorded as a function of threshold energy. This simulation should provide insight into the best contrast that can be expected from a BGO detector based solely on its properties.

As seen in Figure 7, the contrast is a very strong function of the energy threshold. With no threshold, the change in the number of events in pixels adjacent to the edge of the imaged object is quite small. The ratio of the counts in the pixel just before the edge of the object to the counts in the next pixel is only about 1.4. With thresholds of 1 MeV and 2 MeV, the ratio increases to about 5 and 6, respectively. Clearly, the contrast in any real experiment may be significantly reduced from these estimates but it should be equally clear that the use of an energy threshold should greatly assist in ensuring that the goal of achieving an uncertainty of  $\sim 2.5$  mm in the location of the edge of an object can be met.

### 3.5 Crosstalk and shielding

Considering the simplest implementation of our pixelated detector, an important factor limiting performance is the simultaneous energy deposition in adjacent pixels from a single photon interaction, or crosstalk. As a result, we have studied the dependence of crosstalk on various shielding materials and thickness to best isolate individual pixels within the constraints imposed by overall detector efficiency and by the characteristics of commercial photosensors for detection of the scintillation light. Given the nominal pixel size of 5 mm x 5 mm chosen for an initial implementation, we have considered the use of a Hamamatsu H8500C multianode photomultiplier (Hamamatsu Photonics), which provides an 8 x 8 array of 5.8 mm x 5.8 mm anodes. Simulations for monoenergetic pencil beams showed that the total number of counts in the central pixel of an array with dimensions matching closely the photomultiplier characteristics were consistent with the recorded counts in a 3 mm radius cylindrical region in the block of BGO discussed in section 3.2; total energy depositions were also matching closely.

Simulations for a 3 by 3 array were performed with a photon beam that was uniform and incident normally over the central pixel and one half of the grid thickness. Taking advantage of the symmetry of the model, pulse-height spectra were recorded for energy deposition in the central pixel, one adjacent pixel that shared a side with the central pixel, and one corner pixel.

Results from the simulations for the array shielded with 1mm of tungsten and lead are shown in Figure 8 for incident photon energies of 3, 5, and 7 MeV. The pulse-height

1 spectra in the central pixel are essentially identical regardless of the shielding material  
2 and are quite similar to those expected from an unpixelated detector. Full-energy and  
3 single- and double-escape peaks are rather prominent and the continua below the  
4 Compton edge show relatively little energy dependence. The crosstalk in the adjacent  
5 pixel is quite intense below about 0.5 MeV and then decreases fairly rapidly with  
6 increasing energy deposited. For 3 MeV source photons, the energy spectrum of scattered  
7 photons in the adjacent pixel is essentially the same for lead and tungsten. However, the  
8 intensity at the higher photon energies is significantly greater with lead than with  
9 tungsten, i.e., the cross-talk due to 5 MeV source photons shielded by lead is very similar  
10 to that of 7 MeV source photons shielded by tungsten. As expected, the intensity of  
11 crosstalk in the corner pixel is notably smaller, and there is essentially no difference  
12 between the spectra simulated with the two shielding materials. Of particular interest is  
13 the steeper decrease in intensity at energy depositions above about 2 MeV relative to the  
14 adjacent pixel. The difference in counts between the adjacent and corner pixel illustrates  
15 the effect of source energy and pixel location on the crosstalk, in particular the shared  
16 planar boundary between the central and the adjacent pixels.

17 To quantify the effect of shielding on crosstalk, the total number of counts in the  
18 two side-pixels were normalized by the total number of counts in the central pixel.  
19 Without shielding, the crosstalk in the two neighboring pixels is significant even for 1  
20 MeV photons: it is  $\sim 7\%$  in the adjacent pixel and  $\sim 4\%$  in the corner pixel. When the  
21 shielding is 1 mm of tungsten, the crosstalk is decreased to  $\sim 5\%$  in the adjacent pixel and  
22  $\sim 2\%$  in the corner pixel for incident 1 MeV photons. The reader is reminded that these  
23 results are “for a single pixel” and to evaluate the total crosstalk, these values should be  
24 added and multiplied by a factor of four. Clearly the magnitude of the crosstalk is quite  
25 large and will significantly decrease contrast unless lessened by energy discrimination or  
26 the application of electronic filtering.

27 Because the principal source of crosstalk in a pixel is due to the scattering of  
28 incident photons and secondary radiations in adjacent pixels, the effect of crosstalk was  
29 examined by calculating the ratio of counts in an adjacent pixel to the counts in the  
30 central pixel as a function of an energy threshold in the energy range 0 to 4 MeV with  
31 grids of 1 mm thick tungsten or lead. The results for both shielding materials are quite  
32 similar as shown in Figure 9. For source photons of energy greater than the pair  
33 production threshold, the ratios decrease sharply for increasing threshold energy above  
34 0.511 MeV. The effects from pair production can be clearly seen in the simulation for  
35 incident photons of 3 MeV.

36 The total crosstalk in the 3 x 3 BGO array is shown in Figure 10. Clearly, the  
37 shielding afforded by tungsten reduces the crosstalk to the greatest extent. Nevertheless,  
38 as shown in Figure 9 and 10, when weighted by the spectral distribution in a 9 MeV  
39 endpoint energy bremsstrahlung spectrum, both lead and tungsten appear to reduce the  
40 crosstalk in a central pixel from all adjacent pixels to only a few percent.

#### 41 **4. Conclusions**

42 For application to the screening of high-Z objects embedded in the massive  
43 shielding of intermodal cargo containers, it is crucial that the spectral distribution in a  
44 pixelated detector provide sufficient contrast that the dimension of an imaged object can  
45 be accurately defined and that corrections can be made for the fraction of the signal due

1 to scattered photons. The simulations reported here suggest that a pixelated detector  
2 based on an array of BGO crystals, 5 cm thick with pixel dimensions as small as 0.5 cm x  
3 0.5 cm, may provide sufficient contrast to determine the edge of an object with an  
4 average uncertainty of  $\sim 0.25$  cm. Such a detector would meet the desired spatial  
5 resolution of 0.125 in (0.318 cm) stated in the original DHS CAARS specifications.[6]  
6 Although a significant amount of crosstalk will be produced, some shielding combined to  
7 the use of a threshold energy should limit the degradation in contrast to an acceptable  
8 level. In addition to the factors considered here, the performance of the BGO detector  
9 will be affected by the efficiency for collection of scintillation light as well as non-  
10 uniformities in the light sensor. These will be addressed through experimental  
11 investigation.

12 Extraction of accurate linear attenuation coefficients is strongly dependent on the  
13 threshold energy chosen to suppress detected scattered radiation and the signals due to  
14 crosstalk. Assuming a 9 MeV endpoint energy bremsstrahlung spectrum, Quiter showed  
15 that a 3 MeV threshold limited the contribution from scatter predominantly to single-  
16 scattered photons. The current simulations suggest that threshold energies may be further  
17 reduced, possibly down to 2 MeV.

18  
19 BGO operating in pulse counting mode could not be used with current  
20 commercial LINACs, since the pulse structure of such devices ( $\mu\text{s}$ -wide pulse at  $\sim 200$   
21 Hz i.e. operating at a very low duty factor) leads to instantaneous count rates exceeding  
22 by orders of magnitude the capabilities of the relatively slow BGO.[16] However, it is  
23 likely to be sufficiently fast to represent a reasonable detector material for the application  
24 considered here if used with high duty factor systems, such as the current commercial  
25 Rhodotron device running at a low power for inspection of highly-shielded cargos.[9] A  
26 conservative estimate that allows for an upper limit of 2.5% pulse summing during a time  
27 corresponding to three times the decay constant of BGO suggests that interaction rates in  
28 a single pixel of up to  $2.5 \times 10^4 \text{ s}^{-1}$  will be possible. Such low rates should be easily  
29 available with a commercial bremsstrahlung device based on the Rhodotron technology.

## 30 **Acknowledgements**

31 This work performed under the auspices of the U.S. Department of Energy by Lawrence  
32 Livermore National Laboratory under Contract DE-AC52-07NA27344. This work was  
33 funded by a grant of the University Office of the President, University of California,  
34 Berkeley.

## 35 **References**

- 36 [1]. <http://www.marad.dot.gov/statistics>  
37 [2]. S.G. Prussin, et al., Nucl. Instr. and Meth. Phys. Res. A 569 (2006) 853.  
38 [3]. E.B. Norman, et al., Nucl. Instr. and Meth. Phys. Res. A 521 (2004) 608.  
39 [4]. J. Pruet, et al., J. Appl. Phys. 99 (2006) 123102.  
40 [5]. J. Medalia, Detection of nuclear weapons and Materials: Science, Technologies,  
41 Observations, CRS report for congress (2009) R40154.  
42 [6]. Cargo Advanced Automated Radiography System (CAARS) RFP attachment 2  
43 Specifications, (2006) HSHQDC-05-007.

- 1 [7]. CAARS performance specifications—response to vendors comments, U.S. Department of  
2 Homeland Security, (2006) Document No. DNDO PS-100380v3.00.  
3 [8]. <http://www.iba-industrial.com>  
4 [9]. J. Pottier, Nucl. Inst. and Meth. Phys. Res. B 40/41 (1989) 943.  
5 [10]. B. Quiter, et al., J. App. Phys. 103:6 (2008) 064910.  
6 [11]. X5-MCNP-Team, LANL Technical Report (2003) LA-UR-03-1987.  
7 [12]. J. Briesmeister et al., LANL Technical Report (2000) LA-13709-M.  
8 [13]. M.B. Chadwick, et al. NDS, 107 (2006) 12:2931-3118.  
9 [14]. Saint-Gobain, Physical Properties of Common Inorganic Scintillators, Technical  
10 Information, Crystal Properties (2005).  
11 [15]. <http://www.physics.nist.gov/PhysRefData/Star/Text/ESTAR.html>  
12 [16]. P. Metcalfe, T. Kron, P. Hoban, The Physics of radiotherapy X-ray from linear  
13 accelerators, Medical physics, WI, (1997) p21.

1 List of Figures

2 Figure 1. Model of the cubical detector used to estimate the radial dependence of energy  
3 deposition. A monoenergetic pencil beam of photons is centered on and normal to the  
4 front face of the detector. Energy deposition and pulse height spectra are tallied in  
5 cylindrical regions of increasing radii about the beam axis.

6  
7 Figure 2. Model for the estimation of achievable contrast. The detector is a 5 cm cube of  
8 BGO (see Figure 1). A pure absorber shown in black covers the upper-half of the front  
9 face of the detector. Events are tallied in a central column of 1mm x 1mm pixels. Shown  
10 here are two views, a) side-view/cross-section and b) front view with the central line of  
11 pixels

12  
13 Figure 3. Schematic of the front face of the pixelated BGO detector assembly. The pixels  
14 (white) have dimensions 0.5 cm x 0.5 cm x 5 cm long. The 1 mm layer separating each  
15 pixel (grey) was modeled as air, W, Pb, or Pb sandwiched between two layers of plastic.

16  
17 Figure 4. Energy deposition in detectors made of BGO (solid lines) and  $\text{CdWO}_4$  (dotted  
18 lines). The detector is modeled as a 5 cm cube illuminated by a monoenergetic pencil  
19 beam of photons with energies in the range 1 to 9 MeV. The energy deposited by the  
20 photon beam is tallied in a cylindrical region of increasing radius about the beam axis.  
21 The plot represents the total energy deposited within the cylinder of radius  $r$ . The vertical  
22 dashed line highlights the energy deposition within a cylinder of radius  $r = 2\text{mm}$ .

23  
24 Figure 5. Simulations of the energy deposition in a 5 cm cube of BGO illuminated by a  
25 pencil beam incident normal to the center of a face of the cube. The energy deposited was  
26 tallied in a cylindrical region of increasing radius about the beam axis. Upper panel - the  
27 energy deposited relative to the source energy. Lower panel - the energy deposited  
28 divided by the total energy deposited in the cube. The dashed vertical line highlights the  
29 energy deposition within a cylinder of radius  $r = 2\text{mm}$ .

30  
31 Figure 6. Fraction of total counts above a threshold energy as a function of the ratio of  
32 threshold energy to source energy when a monoenergetic pencil beam is incident normal  
33 to the front face of a 5 cm cube of BGO. Results are tallied in a cylindrical region of  
34 radius=3mm centered on the beam axis.

35  
36 Figure 7. Edge detection as a function of energy threshold. The detector model is a 5 cm  
37 cube of BGO irradiated by a uniform beam of bremsstrahlung radiation with dimensions  
38 4 cm x4 cm. The endpoint energy was 9 MeV. A pure absorber covers half of the crystal  
39 and creates an edge at  $x = 0\text{ cm}$  (dotted vertical line).

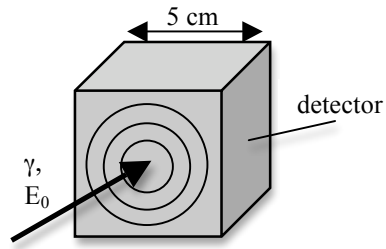
40  
41 Figure 8. Simulated pulse height spectra in three representative pixels of a 3 x 3 pixelated  
42 BGO array. A monoenergetic square beam that covered the central pixel and one half of  
43 the surrounding shielding is incident on the detector. The pulse height spectra incident  
44 photons of 3, 5 and 7 MeV are tallied in the central pixel (top), adjacent pixel (bottom  
45 left), and corner pixel (bottom right) of the array. The shielding consists of 1mm of  
46 tungsten (red full line) or 1mm of lead (black dotted line). Features of the energy spectra  
47 in the central pixel for the 3, 5 and 7 MeV source photons are labeled as follows: f stands

1 for full energy peak, s for single escape peak, and d for double escape peak. Scattered  
2 photons spectra in the adjacent pixel are further identified by the energy of the source  
3 photons and shielding material: Pb (thick arrow) and W (thin arrow).

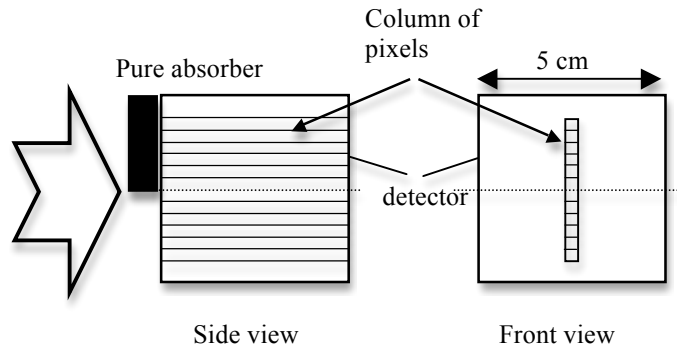
4  
5 Figure 9. Crosstalk in one of the adjacent pixel: the shielding consists in a 1mm layer of  
6 a) W and, b) Pb. A monoenergetic square beam of photon is incident on the central pixel.  
7 Results for a 9 MeV endpoint bremsstrahlung beam are also shown. The total number of  
8 counts in the adjacent pixel is normalized by the total number of counts in the central  
9 pixel.

10  
11 Figure 10. Total crosstalk in the 3x3 BGO array for a 9 MeV endpoint bremsstrahlung  
12 beam. The square beam of photon is incident on the central pixel. The total number of  
13 counts in the surrounding pixels is normalized by the total number of counts in the central  
14 pixel.  
15

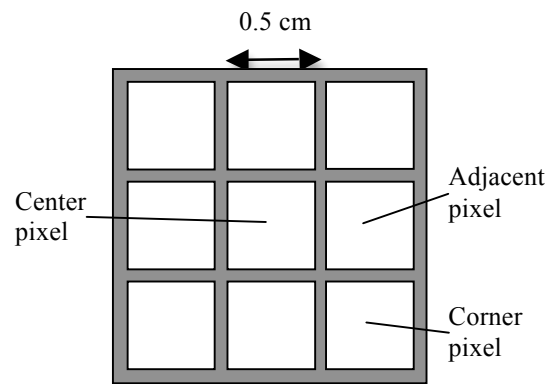
2 [Figure 1.](#)



19 [Figure 2.](#)

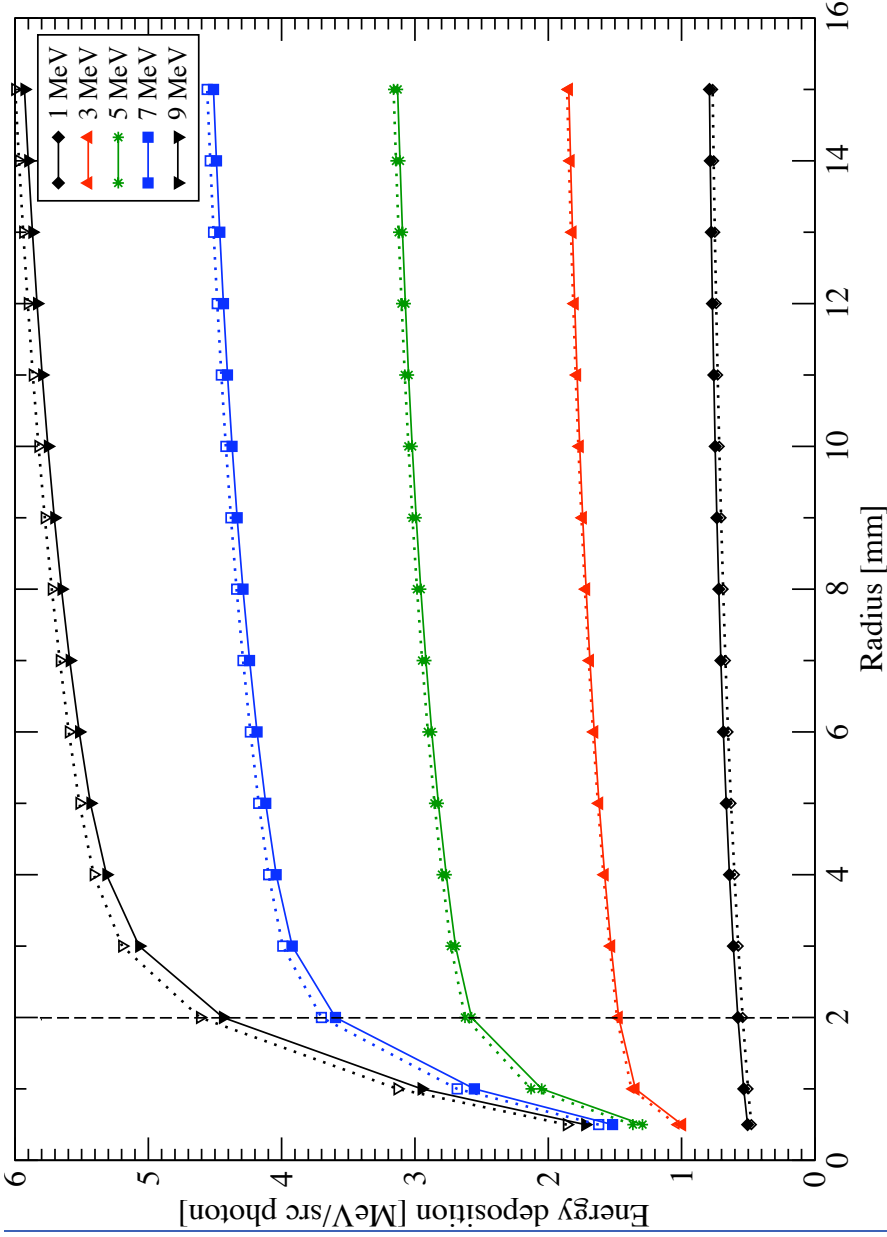


52 [Figure 3.](#)



1  
2

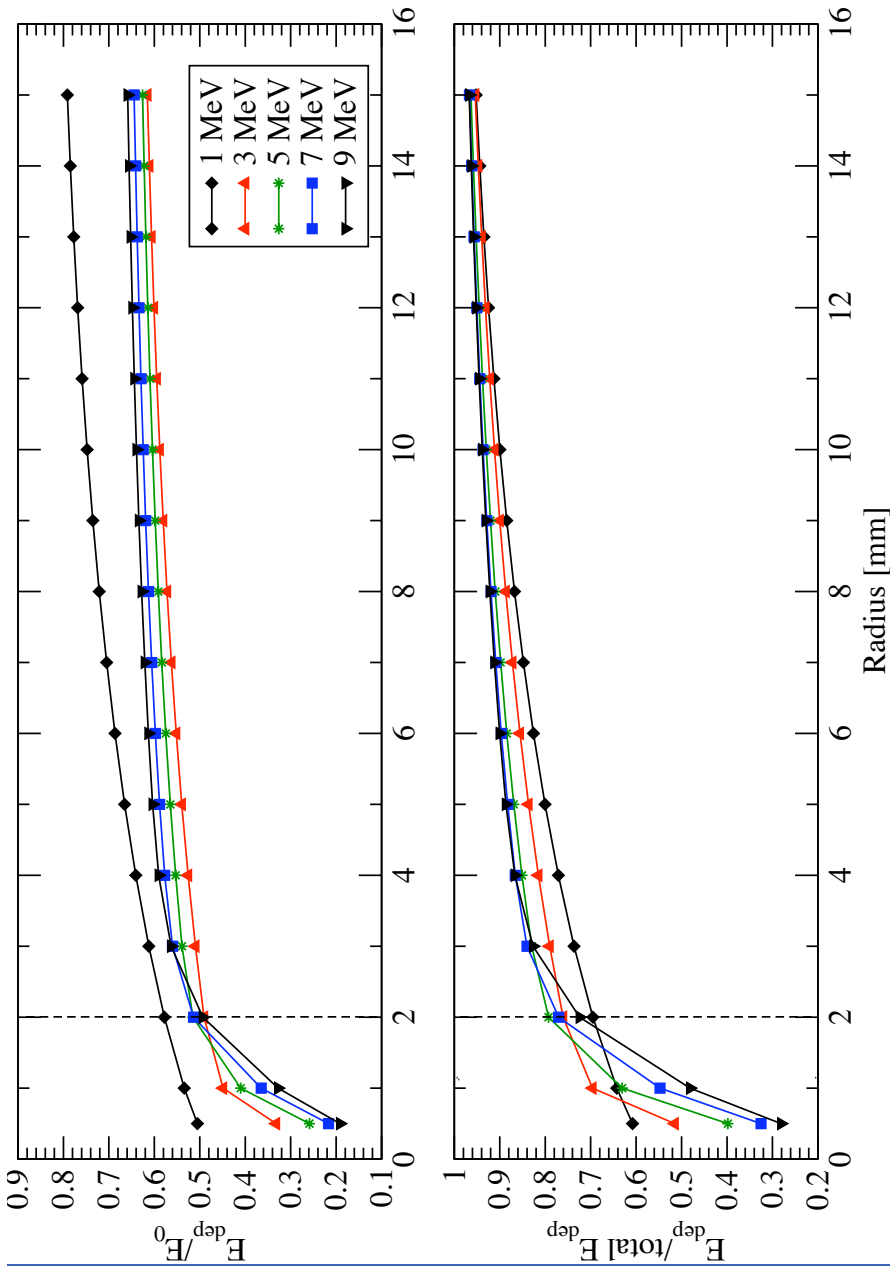
Figure 4.



3  
4  
5  
6  
7  
8  
9  
10  
11  
12  
13  
14

1  
2

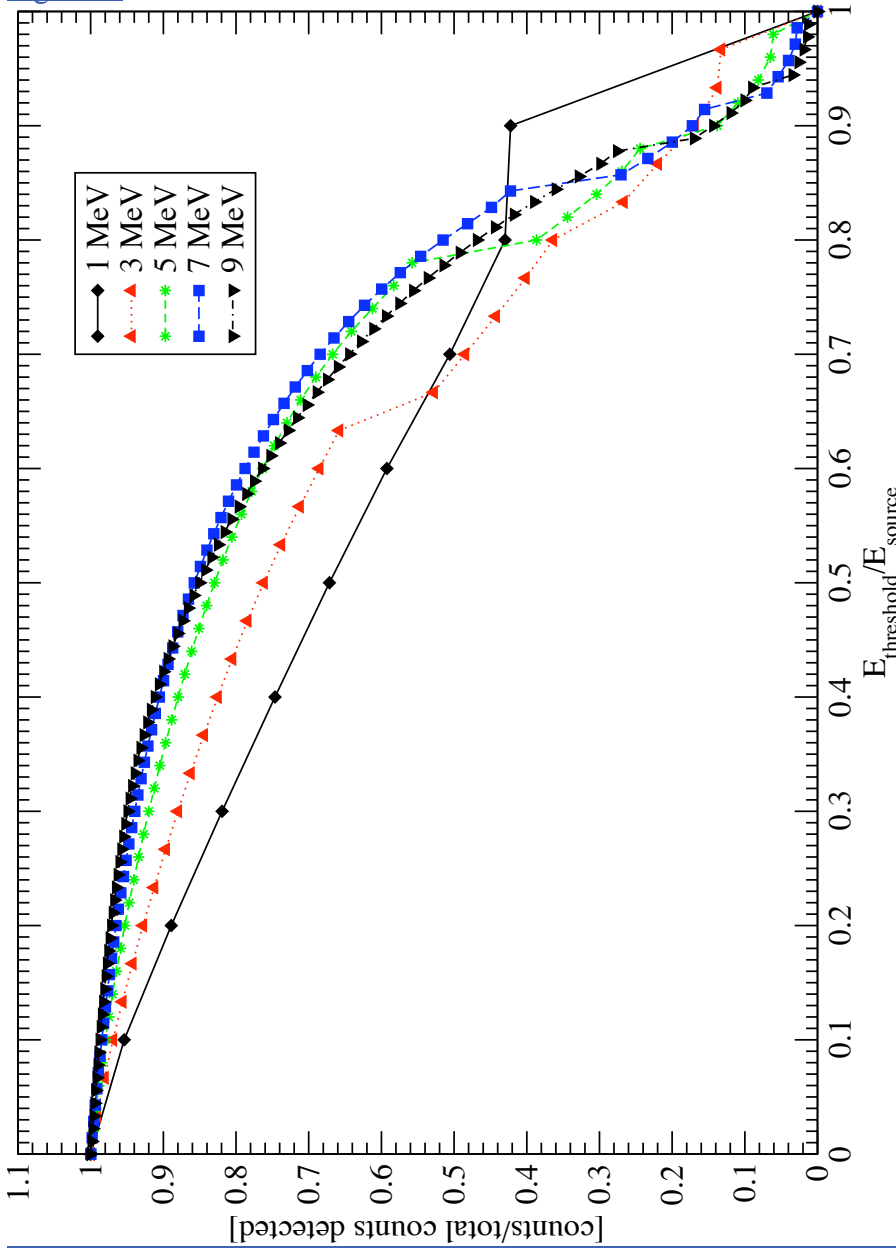
Figure 5.



3  
4  
5  
6  
7  
8  
9  
10  
11  
12  
13

1

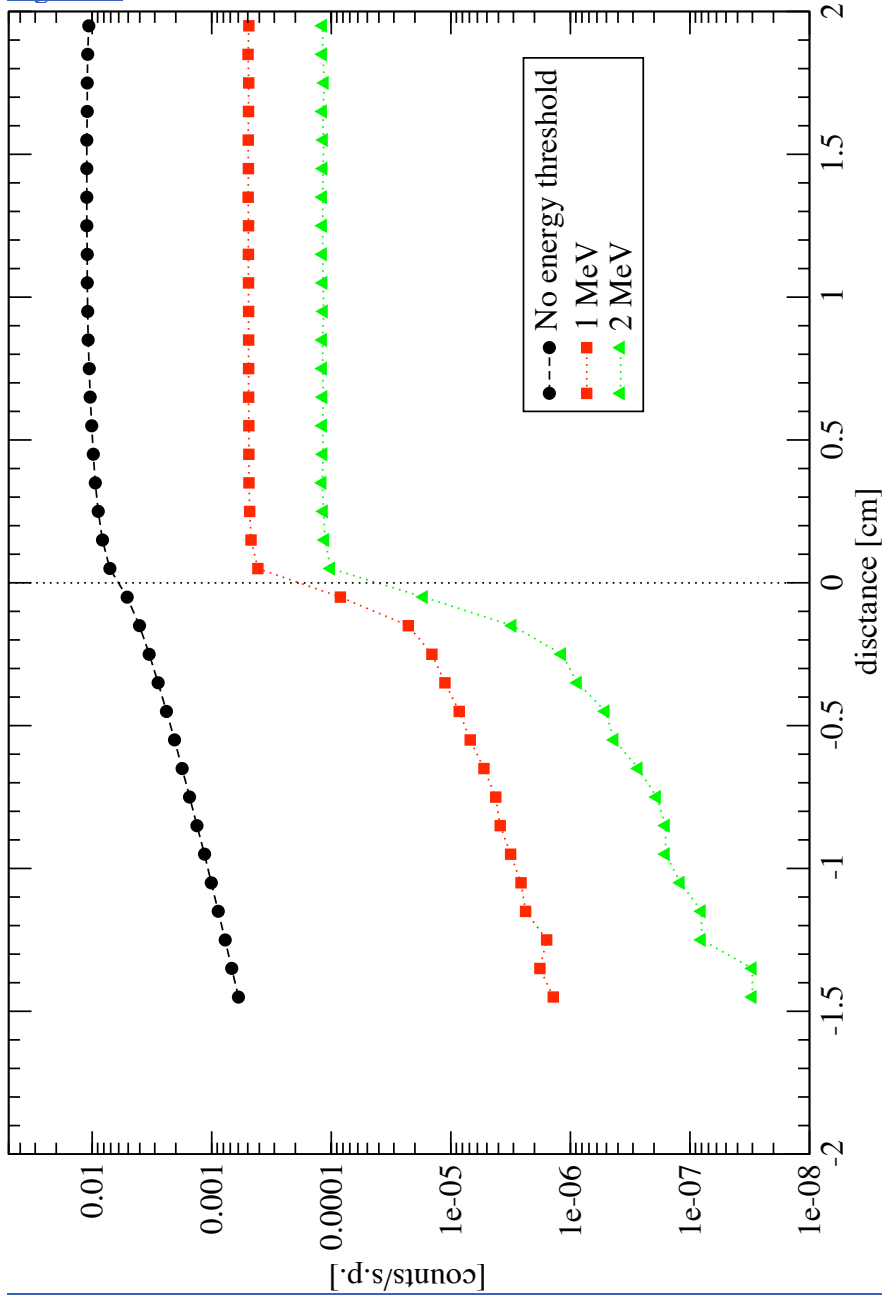
Figure 6.



2  
3  
4  
5  
6  
7  
8  
9  
10  
11  
12  
13  
14

1

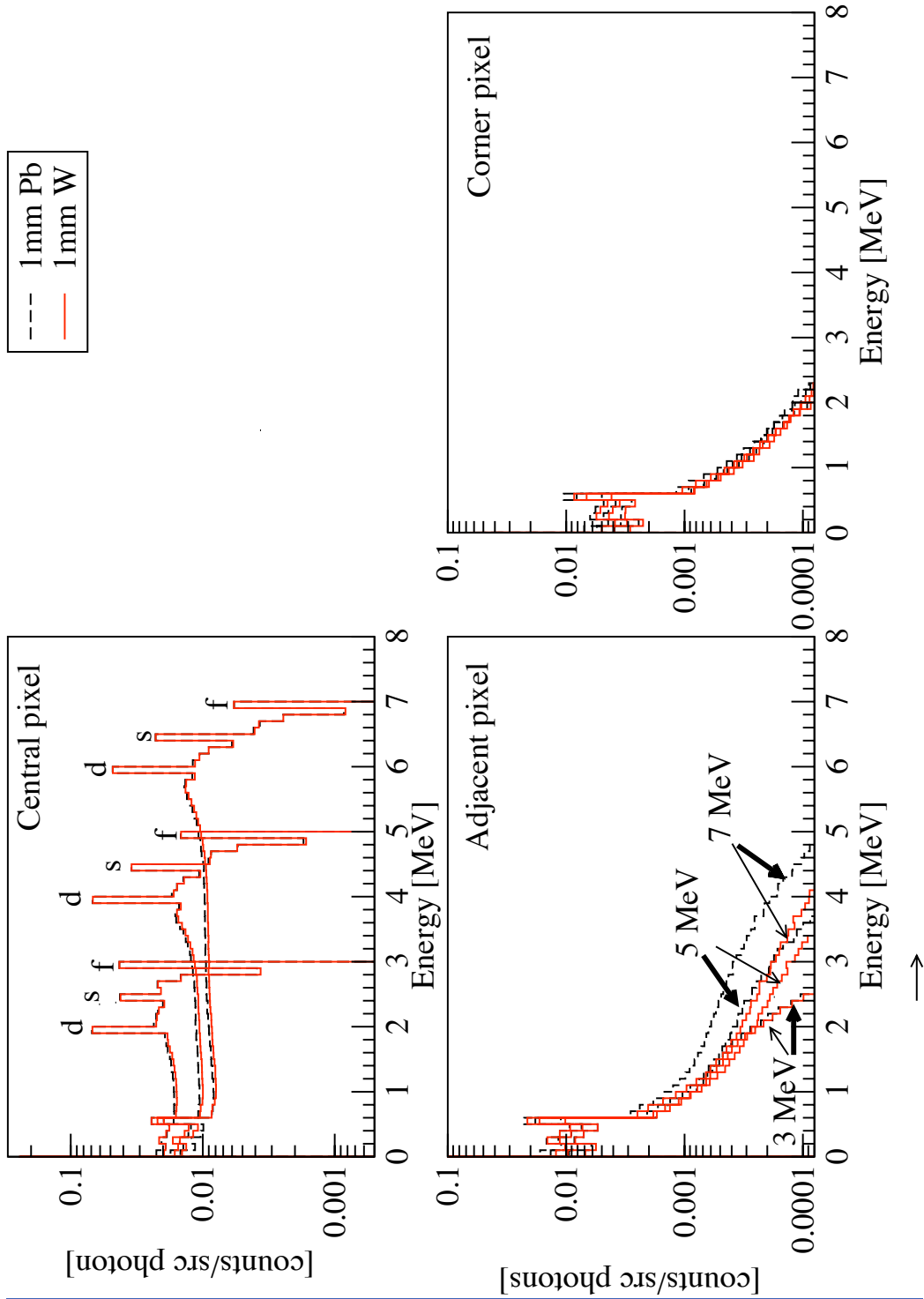
Figure 7.



2  
3  
4  
5  
6  
7  
8  
9  
10  
11  
12

1  
2  
3

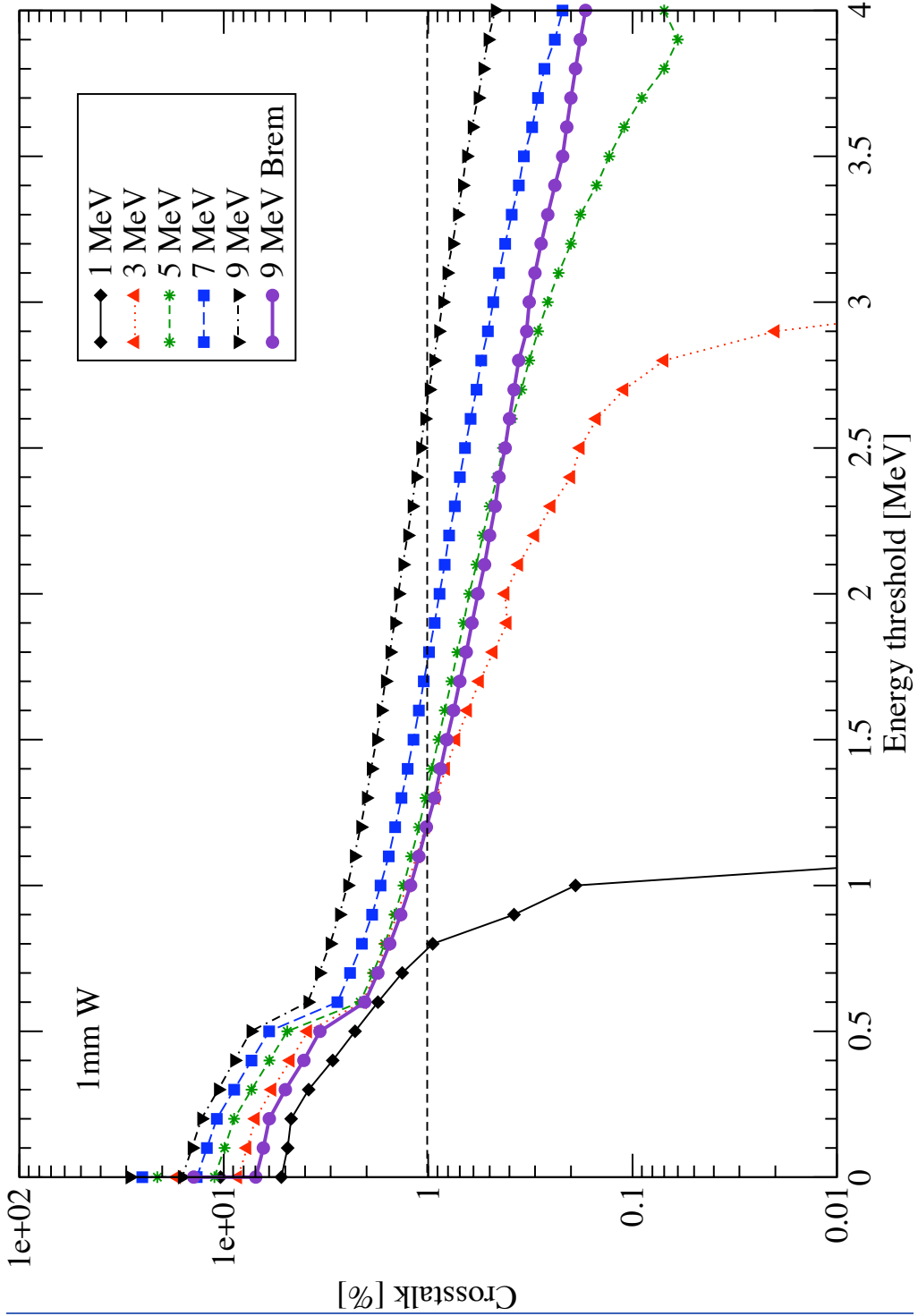
Figure 8.



4  
5  
6  
7

1  
2

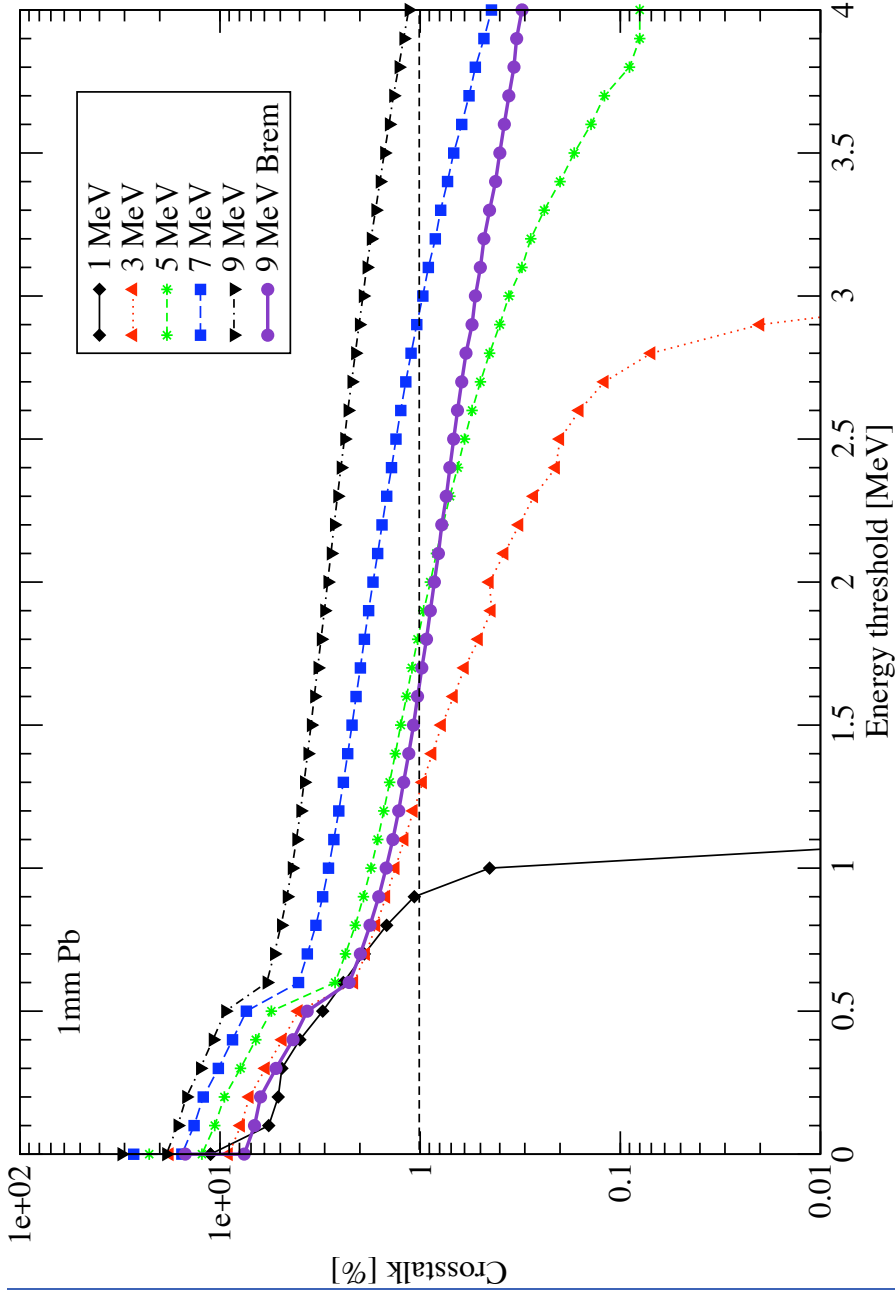
Figure 9a.



3  
4  
5  
6  
7  
8

1  
2

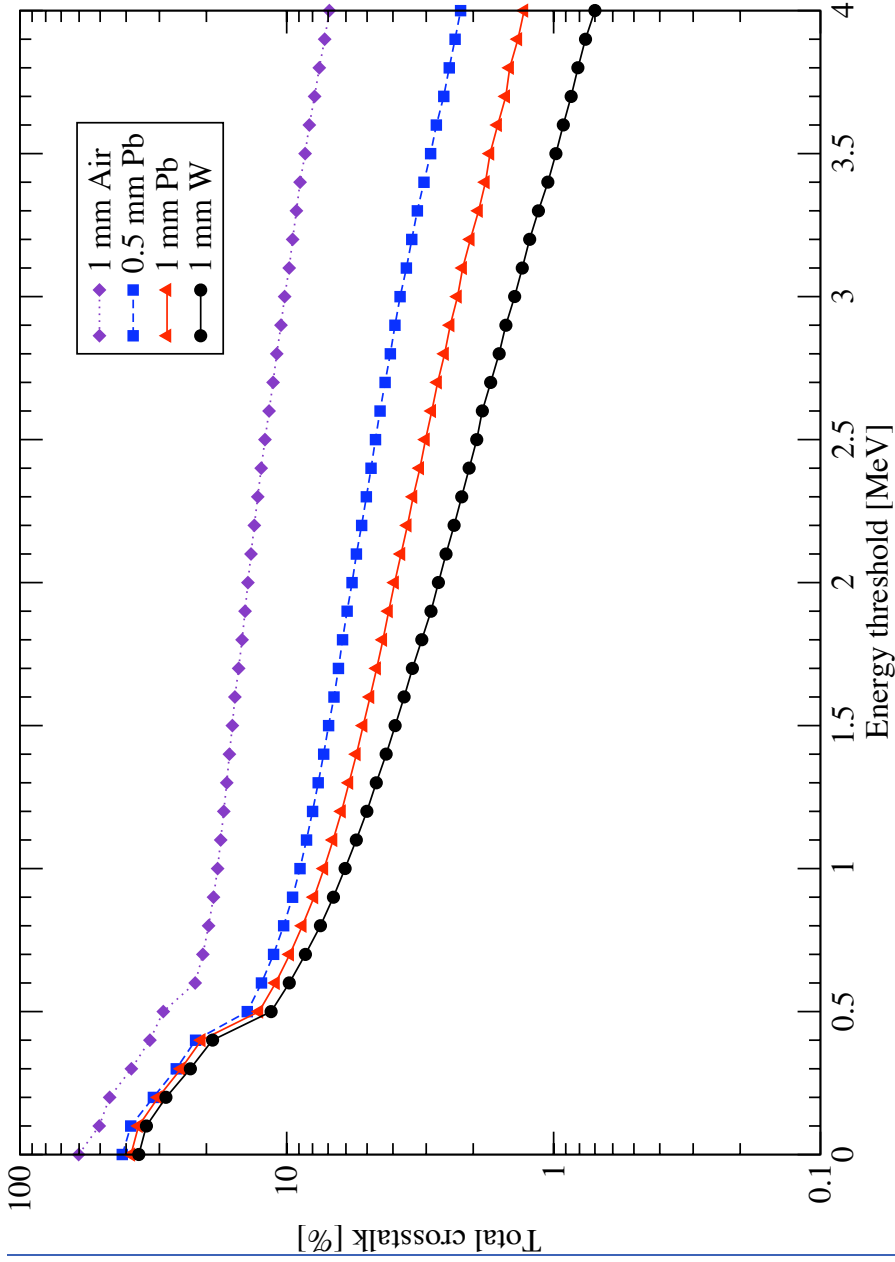
Figure 9b.



3  
4  
5  
6  
7  
8  
9  
10  
11  
12

1  
2

Figure 10.



3  
4